Classical Electrodynamics Coupled to Quantum Mechanics for Calculation of Molecular Optical Properties: a RT-TDDFT/FDTD Approach

Hanning Chen, Jeffrey M. McMahon, Mark A. Ratner, and George C. Schatz*

Argonne−Northwestern Solar Energy Research Center, Department of Chemistry, Northwestern University, 2145 Sheridan Road, Evanston, Illinois 60208

A new multiscale computational methodology was developed to effectively incorporate the scattered electric field of a plasmonic nanoparticle into a quantum mechanical (QM) optical property calculation for a nearby dye molecule. For a given location of the dye molecule with respect to the nanoparticle, a frequency-dependent scattering response function was first determined by the classical electrodynamics (ED) finite-difference time-domain (FDTD) approach. Subsequently, the time-dependent scattered electric field at the dye molecule was calculated using the FDTD scattering response function through a multidimensional Fourier transform to reflect the effect of polarization of the nanoparticle on the local field at the molecule. Finally, a real-time time-dependent density function theory (RT-TDDFT) approach was employed to obtain a desired optical property (such as absorption cross section) of the dye molecule in the presence of the nanoparticle's scattered electric field. Our hybrid QM/ED methodology was demonstrated by investigating the absorption spectrum of the N3 dye molecule and the Raman spectrum of pyridine, both of which were shown to be significantly enhanced by a 20 nm diameter silver sphere. In contrast to traditional quantum mechanical optical calculations in which the field at the molecule is entirely determined by intensity and polarization direction of the incident light, in this work we show that the light propagation direction as well as polarization and intensity are important to nanoparticle-bound dye molecule response. At no additional computation cost compared to conventional ED and QM calculations, this method provides a reliable way to couple the response of the dye molecule's individual electrons to the collective dielectric response of the nanoparticle.

I. Introduction

Optical response is one of the fundamental characteristics of any physical system, usually providing a measure of the charge redistribution induced by an applied radiation field. The perturbation induced by light on a microscopic charge distribution is externally reflected in such macroscopic electromagnetic phenomena as absorption, refraction, luminescence, and scattering of light. In general, no two physical objects exhibit the same optical properties unless they are identical to each other, making the optical spectrum a powerful tool to detect, identify, and measure chemical substances. Among the many optical techniques available nowadays, absorption spectroscopy[1] and Raman spectroscopy[2] are widely used as a result of a number of technological advances, including the development of highly coherent and narrowly diverging monochromatic lasers.[3] A major challenge of Raman spectroscopy is with its feeble sensitivity; however, the amplification of this signal when molecules are adsorbed on silver nanoparticle substrates provides an important technique for circumventing this limitation.[4] Most of this enhancement is now considered to arise from local field enhancement that results from plasmon excitation in the silver particles,[5] although chemical contributions to the enhancement factor likely also exist.

Other examples of photophysical phenomena associated with light interacting with a system composed of plasmonic metal particles and molecules are also of interest. For example, photoinduced electron transfer in a single-molecule-junction (SMJ) has recently gained attention, where it was demonstrated

that switching from conducting to insulating states in a photochromic molecule anchored between two gold electrodes occurs under visible light irradiation.[6] Although the unambiguous observation of photoconductance is rather hard to prove due to associated thermal expansion[7] and charge trapping,[8] it has been argued that the incident light in resonance with electronic transitions between molecule and electrodes can amplify the photocurrent by orders of magnitude when the Fermi energy of the electrode lies between the molecule's HOMO and LUMO.[9] The nonequilibrium Green's function (NEGF) formalism[10] has been generalized for both light absorption[11] and Raman scattering,[12] providing a rationalization for the strong mediation between bridge molecule and metal electrodes that arises from electronic and vibrational couplings. Plasmonic enhancement has also been applied to dye-sensitized solar cells (DSSC),[13] where it has recently been shown that photocurrent can be enhanced by nearly a factor of 10 when the thickness of a TiO_2 layer on the silver particles is reduced from 4.8 to 2.0 nm for a low-efficiency cell.[14]

The development of a theory for processes that couple light both with nanoparticles at the 100 nm size scale and with molecules at the <1 nm size scale is very challenging. Most past work has treated the particle with classical electrodynamics in the absence of the molecule, and then the field arising from plasmonic excitation in the particle is assumed to be applied to the molecule as an external constant field.[15] There have also been studies in which both molecule and particle are treated with quantum mechanics, but these have been limited to particles that are ~100 atoms or smaller.[16] Some hybrid approaches have been proposed in which classical electrodynamics in the particle

* To whom correspondence should be addressed. Fax: 847-491-7713. Phone: 847-491-5657. E-mail: schatz@chem.northwestern.edu.

Calculation of Molecular Optical Properties

J. Phys. Chem. C, Vol. 114, No. 34, 2010 **14385**

has been explicitly coupled to electronic structure calculations in the molecule. These include work by Corni and Tomasi, who described the metal particle polarization effects in the frequency domain by effective charges that were included into molecule's Hamiltonian under the quasi-static approximation.[17] Also, Neuhauser developed a localized two-level random phase approximation (RPA) model to evaluate the molecule's population transfer rate in the presence of surface plasmons (described with FDTD) by means of a density matrix evolution.[18] Most recently Masiello and Schatz applied a many body Green's function method to plasmon-enhanced molecular absorption.[19] In this paper we present a new formalism that couples electrodynamics for the nanoparticle, as described via the finite-difference time-domain (FDTD) method, with electronic structure theory for a nearby molecule that is described using real-time time-dependent density functional theory (RT-TDDFT). The disparate spatial and time scales needed to describe the optical response of the particle and molecule are such that the calculations are done sequentially, and in this version we neglect the "back-coupling"[19] of the molecule on the particle. However the formalism is completely general, providing us with the capability of determining local field enhancement effects on absorption and scattering that include for the wavevector dependence of incident light. In addition, the influence of polarization of the electromagnetic field near the particle surface and its coupling with transition moments associated with excitations in the molecule are automatically taken into account.

In section 2, we briefly describe the RT-TDDFT and FDTD methods, and then the coupling between RT-TDDFT and FDTD through a scattering response function is discussed in detail. In section 3, the hybrid QM/ED method is applied to study (1) surface-enhanced absorption in a system that includes the DSSC ruthenium-based dye molecule N3 and (2) the SERS spectrum of pyridine. A 20 nm diameter silver sphere is used in both applications. In section 4, the applicability of the QM/ED method to linear optical property calculations is validated and its possible extension to nonlinear optics is discussed.

2. Methodology

a. Real-Time Time-Dependent Density Function Theory (RT-TDDFT). For a molecule exposed to a time-dependent external electric field, E_i, along axis i, the dipole moment, P_j, along axis j, in a first-order (linear) approximation is

$$P_j = P_{j0} + \alpha_{ij}E_i \qquad (1)$$

where P_{j0} is the permanent dipole moment and α_{ij} is the linear polarizability tensor. The Einstein summation convention is used in this formula and throughout the paper when appropriate. In the time domain, eq 1 can be written as

$$P_j(t) = P_{j0} + \int dt_1 \alpha_{ij}(t - t_1)E_i(t_1) \qquad (2)$$

where $\alpha_{ij}(t - t_1)$ is related to the frequency domain polarizability via

$$\alpha_{ij}(t - t_1) = \int \frac{d\omega}{2\pi} e^{-i\omega(t - t_1)}\alpha_{ij}(\omega) \qquad (3)$$

Combining eq 2 and eq 3, we obtain

$$P_j(t) = P_{j0} + \int dt_1 \int \frac{d\omega}{2\pi} e^{-i\omega(t-t_1)}\alpha_{ij}(\omega)E_i(t_1) = P_{j0} +$$
$$\int \frac{d\omega}{2\pi} e^{-i\omega t}\alpha_{ij}(\omega)E_i(\omega) \qquad (4)$$

If the induced dipole, $P_j^1(t)$, is defined as

$$P_j^1(t) = P_j(t) - P_{j0} \qquad (5)$$

its frequency domain form is easily recognized as

$$P_j^1(\omega) = \alpha_{ij}(\omega)E_i(\omega) \qquad (6)$$

where

$$\alpha_{ij}(\omega) = \frac{P_j^1(\omega)}{E_i(\omega)} = \frac{\int dt e^{i\omega t}P_j^1(t)e^{-\Gamma t}}{\int dt e^{i\omega t}E_i(t)} \qquad (7)$$

Equation 7 relates a molecule's frequency-dependent polarizability tensor, $\alpha_{ij}(\omega)$, to the evolution of its induced dipole moment, $P_j^1(t)$, under a time-dependent external electric field, $E_i(t)$. Note that we have added a damping factor Γ to eq 7 to reflect the finite lifetime of excited electronic states due to quantum dephasing and vibronic coupling. This ad hoc procedure allows us to incorporate the effect of coupling to the metal particle on the excited state dynamics of the molecule. A more rigorous method for introducing this effect has recently been described,[19] but we have not attempted to implement it here. The ad hoc method is consistent with earlier work using pure QM methods that we used to describe resonance Raman and SERS,[16] and it makes it possible for us to use a relatively short time integration to evaluate optical properties. The commonly used value of 0.1 eV was chosen for Γ in the applications we present below. Note that damping is not applied to the denominator in eq 7 as this is the applied field rather than the polarization response to this field.

Within the framework of density functional theory (DFT), the $\vec{P}(t)$ can be calculated from the perturbed electron density that arises when the system is subjected to an applied field, $\vec{E}_0(t)$, by using the time-dependent Schrödinger equation (TDSE)[20]

$$i\frac{\partial}{\partial t}\varphi(r,t) = \left[-\frac{1}{2}\nabla^2 + \int dr' \frac{\rho(r',t)}{|r - r'|} + \frac{\delta E_{xc}[\rho(r,t)]}{\delta\rho(r,t)} - \vec{E}_0 \cdot \vec{r} \right]\varphi(r,t) \qquad (8)$$

Here the four operators in square brackets on the right-hand side correspond to the kinetic energy, Coulomb repulsion, exchange-correlation energy, and external electric field, respectively. We note that the coupling Hamiltonian between the external electric field and the molecule is given by

$$-\int \varphi^*(r)\vec{E}_0 \cdot \vec{r}\varphi(r)\,dr = -\vec{E}_0 \cdot \int \varphi^*(r)\vec{r}\varphi(r) = -\vec{E}_0 \cdot \vec{P} \qquad (9)$$

where the asterisk indicates the complex conjugate operator. Although an analytical solution is typically not available for the TDSE, it can be propagated by numerical integration

schemes, such as the first-order Crank−Nicholson approximation[21] or the enforced time reversible symmetry (ETRS) algorithm.[22] For an isolated and freely rotated molecule, the absorption cross section $\sigma(\omega)$ can be obtained from[23]

$$\sigma(\omega) = \frac{4\pi\omega}{c}\left\langle\frac{1}{3}(\alpha_{ii}(\omega) + \alpha_{jj}(\omega) + \alpha_{kk}(\omega))\right\rangle_{\text{imag}} \tag{10}$$

where $\langle\rangle_{\text{imag}}$ denotes the imaginary part and c is the speed of light. In addition, the Raman differential cross section for a given vibrational normal mode, p, is provided by[24]

$$\frac{d\sigma}{d\Omega} = \frac{\pi^2}{\varepsilon_0^2}(\tilde{v}_{\text{in}} - \tilde{v}_{\text{p}})^4\frac{h}{8\pi^2c\tilde{v}_{\text{p}}}\left(\frac{45|\alpha_{\text{p}}|^2 + 7\gamma_{\text{P}}^2}{45}\right)\frac{1}{1 - e^{-hc\tilde{v}_{\text{p}}/k_bT}} \tag{11}$$

where || denotes the complex modulus, ε_0 is the vacuum permittivity, $\tilde{v}_{\text{in}}$ is the wavenumber of the incident light, $\tilde{v}_{\text{p}}$ is the wavenumber of the normal mode, h is Planck's constant, k_b is the Boltzmann constant, and T is temperature. In addition, α_{p} and γ_{p} are the isotropic and anisotropic polarizability derivatives, respectively, as shown below

$$\alpha_{\text{p}} = \frac{1}{3}\left(\frac{\partial\alpha_{ii}}{\partial p} + \frac{\partial\alpha_{jj}}{\partial p} + \frac{\partial\alpha_{kk}}{\partial p}\right) \tag{12}$$

$$r_{\text{p}}^2 = \frac{1}{2}\left(\left|\frac{\partial\alpha_{ii}}{\partial p} - \frac{\partial\alpha_{jj}}{\partial p}\right|^2 + \left|\frac{\partial\alpha_{ii}}{\partial p} - \frac{\partial\alpha_{kk}}{\partial p}\right|^2 + \left|\frac{\partial\alpha_{jj}}{\partial p} - \frac{\partial\alpha_{kk}}{\partial p}\right|^2 + 6\left(\left|\frac{\partial\alpha_{ii}}{\partial p}\right|^2 + \left|\frac{\partial\alpha_{jj}}{\partial p}\right|^2 + \left|\frac{\partial\alpha_{kk}}{\partial p}\right|^2\right)\right) \tag{13}$$

b. The Finite-Difference Time-Domain (FDTD) Method. In FDTD simulations, light is assumed incident on a system that is discretized into many small building blocks each characterized by a dielectric permittivity, $\varepsilon(r)$, and a magnetic permeability, $\mu(r)$. Then Maxwell equations[25]

$$\varepsilon(r)\frac{\partial}{\partial t}\vec{E}(r, t) = \nabla \times \vec{H}(r, t) - \vec{J}(r, t) \tag{14}$$

$$\mu(r)\frac{\partial}{\partial t}\vec{H}(r, t) = -\nabla \times \vec{E}(r, t) \tag{15}$$

are solved in the real time domain to obtain the evolution of the electric field, $\vec{E}(r,t)$, magnetic field, $\vec{H}(r,t)$, and electric current density, $\vec{J}(r,t)$. The electromagnetic properties can also be determined in the frequency domain through Fourier transform. To study a broad spectral range, a time-shifted Gaussian wave is typically chosen as the incident field.[26] Since the total electric field, $\vec{E}_{\text{total}}(r,\omega)$, at a given observation point r is a combination of the scattered field, $\vec{E}_{\text{sca}}(r,\omega)$, and the incident field, $\vec{E}_0(r,\omega)$,

$$\vec{E}_{\text{total}}(r, \omega) = \vec{E}_{\text{sca}}(r, \omega) + \vec{E}_0(r, \omega) \tag{16}$$

a scattering response function (SRF), $\lambda(r,\omega)$, can be defined as

$$\lambda_{ij}(r,\omega) = \frac{E_{i,\text{total}}(r, \omega)}{E_{j0}(r, \omega)} - \delta_{ij} \tag{17}$$

Note that $\lambda(r,\omega)$, which provides a measure of local field enhancement, is a complex tensor that depends on both the propagation and polarization directions of the incident light. Normally the light propagation direction is irrelevant in quantum chemistry due to the small size of molecular systems compared to the wavelength of light; however, in the present context where the metal particle is coupled to a molecule, it can play a role as will be demonstrated later.

c. Hybrid Quantum Mechanics/Classical Electrodynamics (QM/ED). Under the assumption of a uniform scattered electric field inside a dielectric building block where the dye molecule is located, the Hamiltonian operator of the dye molecule in the presence of an incident field $\vec{E}_0(t)$ can be rewritten as

$$\hat{H}(t) = -\frac{1}{2}\nabla^2 + \int dr'\frac{\rho(r', t)}{|r - r'|} + \frac{\delta E_{\text{xc}}[\rho(r, t)]}{\delta\rho(r, t)} - \vec{E}_0(t)\cdot\vec{r} - \vec{E}_{\text{sca}}(t)\cdot\vec{r} \tag{18}$$

where the electric field, $\vec{E}_{\text{sca}}(t)$, imposed by the polarized nanoparticle is included. Using the definition of $\lambda(r,\omega)$, $\vec{E}_{\text{sca}}(t)$ can be expressed as a two-dimensional Fourier transform of $\vec{E}_0(t)$ and $\lambda(\omega)$

$$E_{i,\text{sca}}(t) = \frac{1}{2\pi}\int d\omega\, e^{i\omega t}E_{i,\text{sca}}(\omega) =$$
$$\frac{1}{2\pi}\int d\omega\, e^{i\omega t}\sum_j\lambda_{ij}(\omega)E_{j0}(\omega) =$$
$$\frac{1}{2\pi}\int d\omega\, e^{i\omega t}\sum_j\lambda_{ij}(\omega)\int dt_1\, e^{-i\omega t_1}E_{j0}(t_1) =$$
$$\frac{1}{2\pi}\sum_j\int\int d\omega\, dt_1\, e^{i\omega(t-t_1)}\lambda_{ij}(\omega)E_{j0}(t_1) \tag{19}$$

If the incident light is a stepwise pulse with short duration ΔT, where

$$\begin{cases}E_{j0}(t) = E_{j0} & 0 < t < \Delta T \\ E_{j0}(t) = 0 & \text{otherwise}\end{cases} \tag{20}$$

$\vec{E}_{\text{sca}}(t)$ can then be reduced to the one-dimensional Fourier transform of $\lambda(\omega)$, i.e.

$$E_{i,\text{sca}}(t) \approx \frac{1}{2\pi}\sum_j E_{j0}\Delta T\int d\omega e^{i\omega t}\lambda_{ij}(\omega) \tag{21}$$

d. Optical Property Evaluation for a Particle-Coupled Dye Molecule under Irradiation with Fixed Propagation Direction and Randomly Distributed Polarization Direction. As reflected in eq 17 and eq 19, the optical response of a dye molecule bound to a metal particle is a function of the light propagation direction and polarization direction, for example z and x, respectively, through $\lambda(r,\omega)$. In most experimental settings, the relative orientation of the dye molecule with respect to the metal particle is fixed. Without loss of generality, the dye's molecular frame, denoted by three Cartesian axes $\{i,j,k\}$, is assumed to have its k axis to overlap with the light propagation axis z of the experimental frame denoted by $\{x,y,z\}$. Therefore,

Calculation of Molecular Optical Properties

J. Phys. Chem. C, Vol. 114, No. 34, 2010 **14387**

the spatial average of the polarizability tensor diagonal component, $\bar{\alpha}_{xx}$, under the condition of randomly distributed polarization direction is given by

$$\bar{\alpha}_{xx} = \sum_a \sum_b \bar{\alpha}_{ab} \cos(xa) \cos(xb) \tag{22}$$

where $(a,b) \in (i,j,k)$ and xa and xb are the angles between axis x and axis a and b, respectively. Since

$$\cos(xk) = \cos\left(\frac{\pi}{2}\right) = 0 \tag{23}$$

$\bar{\alpha}_{xx}$ can be reduced to

$$\bar{\alpha}_{xx} = \alpha_{ii}\,\overline{\cos(ix)\cos(ix)} + \alpha_{ij}\,\overline{\cos(ix)\cos(jx)} + \\ \alpha_{ji}\,\overline{\cos(jx)\cos(ix)} + \alpha_{jj}\,\overline{\cos(jx)\cos(jx)} \tag{24}$$

After averaging over the rotation angles between the coordinate axes, we end up with

$$\bar{\alpha}_{xx} = \frac{1}{2}(\alpha_{ii} + \alpha_{jj}) = \alpha_k \tag{25}$$

Similarly, the average value of λ_{xx} is given by

$$\overline{\lambda_{xx}} = \frac{1}{2}(\lambda_{ii} + \lambda_{jj}) = \lambda_k \tag{26}$$

Under steady-state conditions, the absorption cross section, $\sigma(\omega)$, of the particle-bound dye molecule is related to its stimulated transition rate, R, and the incident photon flux density, I, using

$$\sigma(\omega) = \frac{R}{I} = \frac{\frac{4\pi E_x}{\hbar\omega}\frac{dP_x}{dt}}{\frac{c}{2\hbar\omega}|E_x|^2} = \frac{4\pi}{c}\left(\frac{2}{|E_x|^2}E_x\frac{dP_x}{dt}\right) \tag{27}$$

where E_x is the electric field imposed on the dye molecule and P_x is its corresponding dipole moment component. For plane-wave incident radiation $E_{x0}\cos(\omega t)$

$$E_x = E_{x0}\cos(\omega t) + E_{x0}|\lambda_{xx}|\cos(\omega t - \varphi) \tag{28}$$

$$P_x = P_{x0} + |\alpha_{xx}|E_{x0}\cos(\omega t - \theta) \tag{29}$$

where φ and θ represent the phase shift of scattering response function λ and polarizability α relative to incident light, respectively. After some mathematical manipulations

$$\sigma(\omega) = \frac{4\pi\omega}{c}(|\alpha_{xx}|\sin\theta + |\alpha_{xx}||\lambda_{xx}|\sin\theta\cos\varphi - \\ |\alpha_{xx}||\lambda_{xx}|\cos\theta\sin\varphi) = \frac{4\pi\omega}{c}(\langle\alpha_{xx}\rangle_{\text{imag}} + \langle\alpha_{xx}\lambda_{xx}^*\rangle_{\text{imag}}) = \\ \frac{4\pi\omega}{c}\langle\alpha_{xx}(1 + \lambda_{xx}^*)\rangle_{\text{imag}} \tag{30}$$

In the molecular frame, the absorption cross section $\sigma_k(\omega)$ for a bound dye molecule irradiated by light with fixed propagation direction k is

$$\sigma_k(\omega) = \frac{4\pi\omega}{c}\left\langle\alpha_k(1 + \lambda_k^*) + \frac{1}{8}\gamma_k\right\rangle_{\text{imag}} \tag{31}$$

where the anisotropic polarizability is

$$\gamma_k = (\alpha_{ii} - \alpha_{jj})(\lambda_{ii}^* - \lambda_{jj}^*) + (\alpha_{ij} + \alpha_{ji})(\lambda_{ij}^* + \lambda_{ji}^*) \tag{32}$$

Following a similar procedure, the Raman differential cross section, $d\sigma/d\Omega$, of such a bound dye molecule can be inferred following Long[27]

$$\frac{d\sigma}{d\Omega} = \frac{\pi^2}{\varepsilon_0^2}(\tilde{\nu}_{\text{in}} - \tilde{\nu}_{\text{p}})^4\frac{h}{8\pi^2c\tilde{\nu}_{\text{p}}}\left|\frac{8\alpha_{k,\text{p}} + \gamma_{k,\text{p}}}{8}\right|^2\frac{1}{1 - e^{-hc\tilde{\nu}_{\text{p}}/k_{\text{b}}T}} \tag{33}$$

where the isotropic polarizability derivative, $\alpha_{\text{p},k}$, and the anisotropic polarizability derivative, $\gamma_{\text{p},k}$, are defined as

$$\alpha_{\text{p},k} = (1 + \lambda_k)\frac{\partial\alpha_k}{\partial p} \tag{34}$$

and

$$\gamma_{\text{p},k} = \left(\left(\frac{\partial\alpha_{ii}}{\partial p} - \frac{\partial\alpha_{jj}}{\partial p}\right)(\lambda_{ii} - \lambda_{jj}) + \left(\frac{\partial\alpha_{ij}}{\partial p} + \frac{\partial\alpha_{ji}}{\partial p}\right)(\lambda_{ij} + \lambda_{ji})\right) \tag{35}$$

Note that the $(1 + \lambda_k)$ term in eq 34 is evaluated at the Stokes frequency while the polarizability derivative term is at the incident frequency. In our evaluations we assumed the zero Stoke's shift limit of this expression.

3. Numerical Results

a. Scattering Response Function of a 20 nm Diameter Silver Sphere. In this first application, we study the effect of polarization on the field enhancement factor $\lambda(r,\omega)$ as defined in eq 17 for the scattering of light from a sphere. For a 20 nm diameter silver sphere centered at $(0, 0, 0)$, $\lambda(r,\omega)$ was calculated by FDTD for each of five observation points: $(11, 0, 0)$, $(12, 0, 0)$, $(13, 0, 0)$, $(14, 0, 0)$, and $(15, 0, 0)$. Please note that a Cartesian coordinate system with a unit length of 1 nm was used in all of our calculations involving the silver sphere. The light propagation direction is fixed along the $+z$ axis in all FDTD simulations, which were performed using the JFDTD3D package.[28] A small grid size of 0.25 nm was chosen to smoothly discretize a cubic simulation box with a side length of 40 nm, making a total of 4096000 grid cells. Each grid cell is characterized by ε and μ values based on its distance to the center of the silver sphere. The values of ε and μ for silver were determined from experiment,[29] while they are ε_0 and μ_0 in vacuum, respectively. The incident light pulse was injected from the plane at $z = -16$ using the functional form

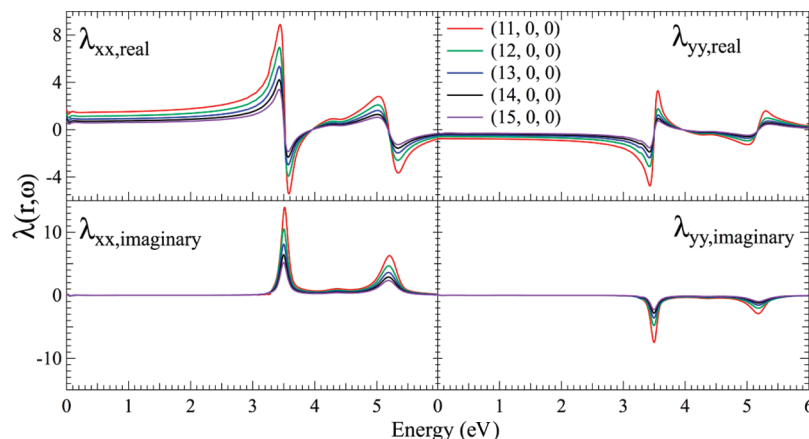$$E_0(t) = e^{-(t-t_0)^2/\sigma^2}\sin(\omega_0 t) \tag{36}$$

Figure 1. The tensor components of the scattering response function, $\lambda(r,\omega)$, at five observing points close to a 20 nm diameter silver sphere centered at (0, 0, 0).

where $t_0 = 10.0$ fs, $\sigma = 0.7$ fs, and $\omega_0 = 600.0$ nm. The parameters of the incident pulse were carefully chosen to fully cover the visible spectrum from 300 to 800 nm. Perfectly matched layers were placed above and below boundary planes $z = -20$ and $z = +20$ to remove reflection, while a two-dimensional periodic boundary condition was applied along the x axis and y axis. A time step of 4.57×10^{-4} fs and a total simulation time of 100 fs were employed so that the calculated scattering response functions converged to $\pm 0.2\%$ in terms of relative uncertainty. At each observation point, two separate FDTD calculations were carried out with different pulse polarization directions, one along the x axis and the other along the y axis. During the calculations, the electric field vectors at the five observation points were saved every 10 time steps for postprocessing, which eventually enabled us to determine $\lambda(r,\omega)$ by Fourier transform according to eq 17.

Our results indicate that the scattered field along the pulse polarization direction is much stronger than that along the two other directions by at least 2 orders of magnitude for the silver sphere, making the off-diagonal terms in $\lambda(r,\omega)$ nearly negligible compared to the diagonal terms. Therefore, only the diagonal terms in $\lambda(r,\omega)$ are presented in Figure 1 and were used later to evaluate the time-dependent scattered field in the RT-TDDFT calculations given by eq 19. Note that the $\lambda(r,\omega)$ was truncated at 6.0 eV to fulfill the requirement of FDTD that the wavelength must be long relative to the grid size for a uniform electromagnetic field inside a grid. The figure shows that the real parts of λ_{xx} and λ_{yy} exhibit two dip-peak features centered at ∼3.4 and ∼5.2 eV, while their imaginary parts display two peaks at the same locations. For the imaginary parts, which are pertinent to light absorption, the sharper and stronger peaks at 3.4 eV can be ascribed to an intraband transition (plasmon excitation) whereas the broader and weaker peaks at 5.2 eV are induced by an interband transition. Interestingly, the sign of $\lambda_{xx,\text{imag}}$ is opposite to that of $\lambda_{yy,\text{imag}}$ for both peaks. The positive value of $\lambda_{xx,\text{imag}}$ indicates that the corresponding scattered field, $E_{\text{sca},xx}$, lags behind the incident light. On the other hand, the negative value of $\lambda_{yy,\text{imag}}$ suggests that $E_{\text{sca},yy}$ leads the incident light in phase. Outside the two peak regions, the values of $\lambda_{xx,\text{imag}}$ and $\lambda_{yy,\text{imag}}$ are close to zero, indicating that there is neither energy loss nor phase change of the incident light at off-resonance frequencies. Similarly, $\lambda_{xx,\text{real}}$ and $\lambda_{yy,\text{real}}$ exhibit opposite peak patterns at the two resonance frequencies. Given the geometric symmetry of the silver sphere, with total induced dipole moment parallel to the incident light polarization direction, it is not surprising that the strength of λ_{xx} is significantly larger than that
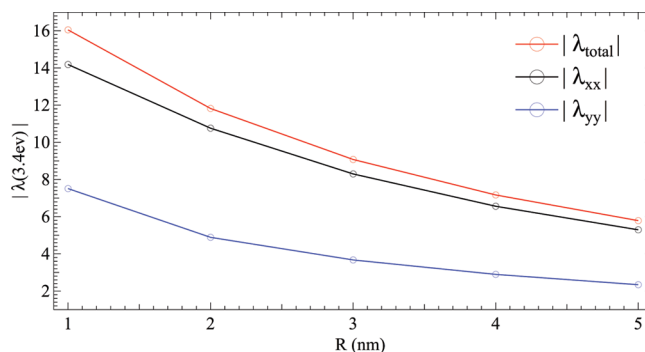

Figure 2. Strength of the on-resonance scattering response function, $\lambda(r, 3.4$ eV$)$, as a function of R, the distance from the observing point to the particle's surface.

of λ_{yy} at any given observation point along the x axis. Nevertheless, λ_{yy} is not negligibly small compared to λ_{xx}, particularly when the observation point is within 2.0 nm of the silver sphere surface. Figure 2 shows the decay of $\lambda(r, 3.4$ eV$)$ at the plasmon frequency with increasing distance from the observation point to the particle's surface. As the observation point moves from (11, 0, 0) to (15, 0, 0), in addition to a 50% drop in the total scattered field strength defined by

$$|\lambda_{\text{total}}| = \sqrt{\lambda_{xx}^2 + \lambda_{yy}^2} \tag{37}$$

$|\lambda_{xx}|$ was observed to decay slightly faster than $|\lambda_{yy}|$. Moreover, the imaginary part was shown to contribute more significantly to either $|\lambda_{xx}|$ or $|\lambda_{yy}|$ than the real part. Since $|\lambda_{\text{total}}|$ is still as large as ∼8 even for the most distant observation point of (15, 0, 0), the 20 nm diameter silver sphere is an ideal model system to investigate plasmonic enhancement for absorption and Raman spectra as discussed in the next two subsections.

b. Absorption Spectra of N3 Dye. *cis*-Bis(isothiocyanato)-bis(2,2′-bipyridyl-4,4′-dicarboxylato)-ruthenium(II), known as N3,[30] is one of the most widely used charge transfer sensitizers in DSSC due to its high extinction coefficient and extraordinary chemical stability.[31] More impressively, the N3 dye is capable of transferring its excited electrons to a TiO$_2$ layer within femtoseconds, much faster than other competing deactivation processes.[32] Recently, a strong dependence of the N3 dye's incident photon conversion efficiency (IPCE) on the thickness of a TiO$_2$ layer[14] which separates the dye and the underlying silver NPs was revealed, suggesting the possibility to signifi-
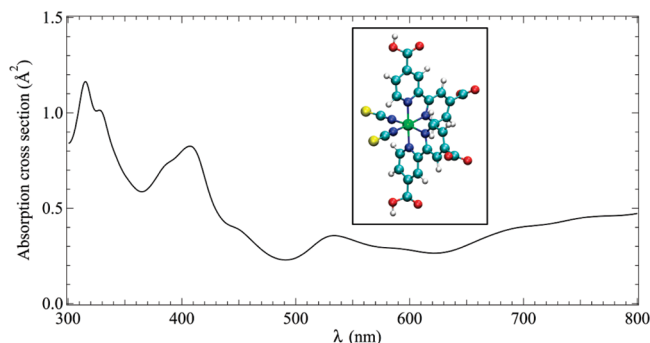
Calculation of Molecular Optical Properties

J. Phys. Chem. C, Vol. 114, No. 34, 2010 **14389**

Figure 3. Calculated absorption profile of the bare N3 dye (molecular structure illustrated in the inset).

Figure 4. Calculated absorption profile of a silver-bound N3 dye with different values of the dye−particle separation, *R*. The system setup is illustrated in the inset.

cantly improve the dye molecule's light absorption through plasmonic enhancement.

For the isolated N3 dye with a neutral charge, the structure was first optimized by a ground-state DFT calculation using the Goedecker−Teter−Hutter (GTH) dual-space Gaussian pseudo-potential,[33] which was parametrized with the Perdew−Burke−Ernzerhof (PBE) exchange-correlation functional.[34] A polarized-valence-double-ζ (PVDZ)[35] basis set was chosen and the wavelet Poisson solver[36] was applied to treat electrostatic interactions under nonperiodic boundary conditions. All DFT simulations were performed using the CP2K molecular simulation package.[37] After geometry optimization, three separate RT-TDDFT simulations were carried out, each with a stepwise electric field pulse (i.e., eq 20) applied along one of the three coordinate axes. The electric field pulse had a magnitude of 0.02745 V·nm^{-1} and a duration time of 0.0121 fs. The field is evaluated at the center of mass of the molecule for the RT-TDDFT calculation. Field gradient effects were found to be negligible for this application. The wave function of the system was propagated for 4000 steps according to the TDSE using the ETRS algorithm[22] with a time step of 0.0121 fs. Then the polarizability tensor was calculated using eq 7 and the light absorption cross section was in turn determined according to eq 10. The absorption cross section for bare N3, presented in Figure 3, shows N3 as a wide spectrum light harvester, covering the whole visible range. The maximum cross section of 1.17 Å^2 occurs for the sharp peak at 315 nm, which also exhibits a small shoulder at 328 nm. In addition, there is a moderately broad peak at 407 nm with a peak value of 0.83 Å^2. The broadest absorption band, ranging from 530 to 800 nm, has an average absorption cross section of 0.4 Å^2. Compared to experimental measurements,[14] our calculated absorption profile is shifted toward the red by 20 nm on average, primarily due to the incorrect asymptotic behavior of our short-ranged DFT functional. Although the underestimated HOMO−LUMO gap typically encountered in DFT calculations[38] can be partially improved by adding long-range corrections, such as via the statistical averaging of orbital potentials (SAOP),[39] the associated computational cost is prohibitively expensive for RT-TDDFT. The same can be said about improvements on the PVDZ basis. However, in light of our reasonably good results, no effort was invested in achieving better Kohn−Sham orbital energies.

For the silver-bound N3 dye as illustrated in the inset of Figure 4, the system is set up such that one of the four carboxyl groups points toward the center of the silver sphere to mimic the binding orientation of the N3 dye on a semiconductor surface as revealed by earlier studies.[40] In addition, the aromatic plane of the binding bipyridine group is normal to the *z* axis. The ruthenium atom, which was assumed to be the molecule's center of mass (COM), was placed at the above-mentioned observation points. Since even the long axis of the N3 dye is only 0.8 nm,
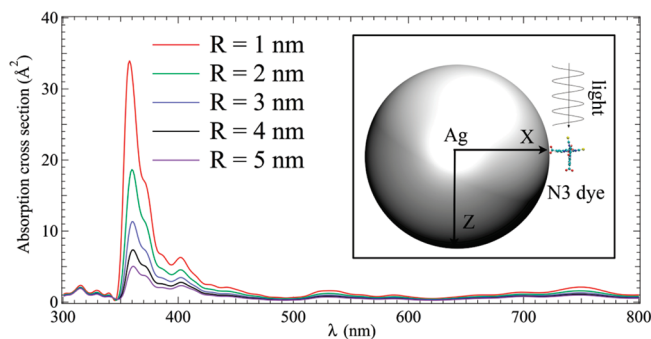
the scattered field, E_{sca}, imposed on it is regarded as spatially homogeneous. For a given observation point, E_{sca} was deter-mined according to eq 21 using the same E_0 applied to the isolated N3 system together with the corresponding $\lambda(r,\omega)$ as previously discussed. Subsequently, two independent RT-TDDFT simulations were performed with the added E_{sca}. The polarization direction associated with E_0 is along the *x* axis and *y* axis in the first and second simulations, respectively. In a similar manner to the isolated N3 dye, the system's induced dipole was saved before it was used to evaluate the absorption cross section using eq 31. As presented in Figure 4, the formation of a sharp peak at 357 nm (equivalent to 3.48 eV) is the primary consequence of plasmon enhancement on light absorption. However note that the cross section is significantly amplified at nearly all visible frequencies. The width of the 357 nm peak is approximately 50 nm, which is consistent with the peak width of $\lambda(r,\omega)$ as depicted in Figure 1. Therefore, at the peak location, the primary absorption peak can be ascribed to strong coupling between the electronic transitions of the N3 dye and the plasmon oscillations of silver sphere. More interestingly, silver binding not only increases the absolute values of absorption cross section but also changes the relative height of the different absorption peaks. For example, the peak at 311 nm, which is at least 50% stronger than other peaks for the isolated N3 molecule, is now nearly as intense as the broad absorption band ranging from 500 to 800 nm. In addition, the absorption peak at 407 nm is significantly amplified and is second only to the 357 nm resonance peak in the presence of the silver sphere.

Regardless of the underlying physical mechanisms, the absorption enhancement effect can be quantified by calculating the ratio of $\sigma_{bound}(\omega)$ and $\sigma_{isolated}(\omega)$, the absorption cross sections for silver-bound and isolated N3 dye, respectively. As exhibited in Figure 5, the enhancement is strongest at the plasmon resonance wavelength of 360 nm. When the N3 dye is only 1 nm away from the silver surface, the on-resonance enhancement ratio reaches a maximum value of ∼55. This value is roughly proportional to $|\lambda + 1|^2$, although there is a prefactor which reflects polarization effects. The corresponding maximum absorption cross section of ∼34 Å^2 is not easily attainable by any bare organic sensitizer with a molecular size similar to N3. On the red side of the plasmon frequency, the absorption enhancement ratio exhibits peaks at 407, 440, 530, and 750 nm, leading to the enhanced absorption peaks at those four wave-lengths. Interestingly, there is little or weak at best absorption enhancement on the blue side of the plasmon frequency where the enhancement ratio is close to 1. Even when the N3 dye and the silver sphere are 5 nm apart, the corresponding on-resonance enhancement ratio at 360 nm is larger than 8. As anticipated,
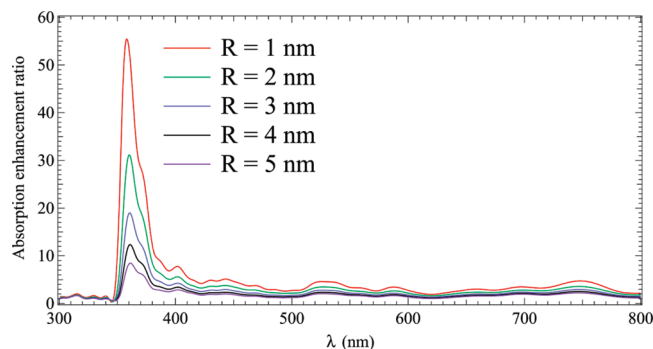
Figure 5. The dependence of the computed absorption enhancement ratio on dye−particle separation, R.
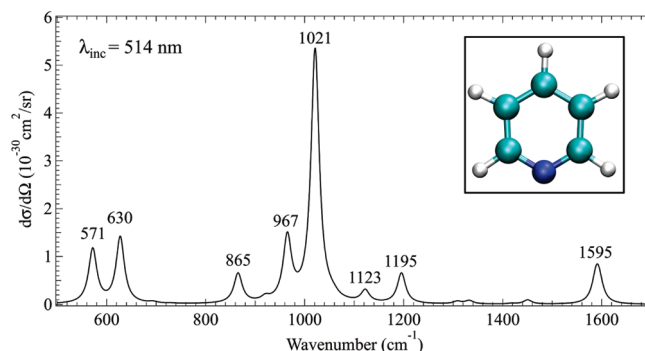

Figure 6. Calculated normal Raman spectrum of isolated pyridine. All peaks were broadened by a Lorentzian function with a width of 10 cm^{-1}.
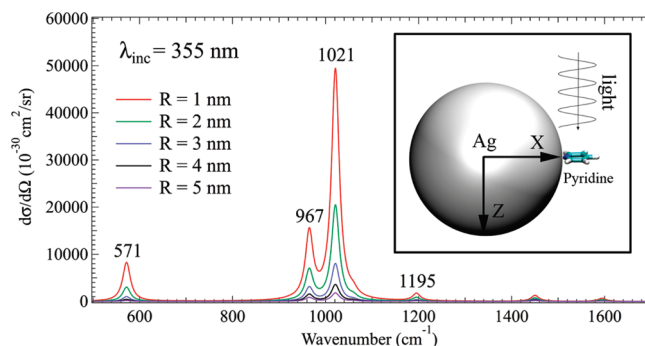

Figure 7. Computed surface-enhanced Raman spectrum of silver-bound pyridine. The composite system is depicted in the inset.

both the absorption profile and the enhancement ratio are monotonically decreasing functions of the dye−particle separation over the entire visible range, demonstrating a distinct advantage of diminishing the protective layer thickness in the plasmonic DSSC.[14]

c. Raman Spectra of Pyridine. Pyridine has been used as a model system to study the interaction between an analyte molecule and a plasmonic surface since the early development of SERS due to its easily assignable vibrational modes and considerable signal amplification.[41] In the present study, a vibrational mode analysis was first performed on the optimized geometry of an isolated pyridine molecule to determine its normal mode vectors and frequencies by diagonalizing the Hessian matrix constructed after geometry optimization. A total of 27 normal vectors were ascertained. Afterward, an RT-TDDFT simulation was carried out on each of the 27 perturbed pyridine geometries, which were built from the optimized geometry by adding the corresponding normal mode vectors. A stepwise electric field with a magnitude of 0.02745 fs and a time duration of 0.0242 fs was applied at the beginning of each simulation to trigger the wave function propagation. The field is evaluated at the center of mass of the molecule. Field gradient effects were found not to be important in this application, so they were neglected. Each RT-TDDFT trajectory is 48.36 fs long, and a time step of 0.0242 fs was used. Once again, the GTH pseudopotential[33] and PBE functional[34] were chosen to model the core−valence and exchange-correlation interactions, respectively. The derivatives of the polarizability tensor with respect to the normal coordinates were evaluated through numerical differentiation prior to the calculation of differential Raman cross section for isolated pyridine according to eq 11. The wavelength of the incident light for modeling the Raman experiments was chosen to be 514 nm.[4] The result for isolated pyridine is presented in Figure 6. This shows a pronounced peak at 1021 cm^{-1} as well as seven modest peaks at 571, 630, 865, 967, 1123, 1195, and 1595 cm^{-1}. The locations of the primary peak and its closest secondary peak attributed to ring breathing are very close to the experimental values[4] of 1030 and 991 cm^{-1}. (These can be slightly varied through solvent effects.)[42] However, the height of the 967 cm^{-1} peak is apparently underestimated compared to the experiment results in which it is nearly as strong as the 1021 cm^{-1} peak. This underestimation is likely due to limitation in the accuracy of the underlying exchange-correlation functionals and core−valence pseudopotentials. Nevertheless, our simulations properly exhibit stronger intensities for the two ring-breathing vibrational modes than the others. The cross section values of ~10^{-30} cm^2/sr are similar to previous estimates and illustrate why normal Raman is not suitable for ultratrace or single-molecule detection.[43]

To investigate plasmon enhancement of the Raman spectrum of pyridine, a 20 nm silver sphere was placed near the pyridine (inset of Figure 7) in such a way that the sphere center, the nitrogen, and the para-carbon atoms of pyridine were all along the x axis. The normal vector to the pyridine ring is along the z axis, which is also the propagation direction of the incident light. The plasmon−dye separation, R, is defined as the distance between the silver surface and the pyridine ring center. A total of five simulations with uniformly spaced values of R from 1.0 to 5.0 nm were carried out. In each QM/ED simulation, we followed the same procedure as that for the bare pyridine except for the presence of an external scattered field, E_{sca}, which was determined according to eq 21 using the values of $\lambda(r,\omega)$ as discussed in subsection 3(a). In addition, the incident light was polarized only along x axis or y axis, and the differential Raman cross section was evaluated by eq 33 assuming a uniformly distributed experimental light polarization direction on the xy plane of the molecular frame. It turns out that the Raman signals of the five simulations are all maximally amplified when $\lambda_{inc} =$ 355 nm, coincident with the plasmon wavelength of the silver sphere. Therefore, the SERS spectrum of pyridine was calculated with that incident wavelength and is presented in Figure 7. Besides the two central peaks, enormous enhancement was observed for the two peaks at 571 and 1195 cm^{-1}; these refer to ring-deformation and ring-stretch modes, respectively, as illustrated in Figure 8. Very encouragingly, the emergence of the two secondary peaks is consistent with the experimental finding.[44] Moreover, the large amplification of the 571 cm^{-1} mode can be partially ascribed to the nitrogen and para-carbon atoms that vibrate toward the silver sphere to couple with the induced plasmon field, whereas these two atoms are nearly stationary for the 1195 cm^{-1} mode. The strong coupling is also reflected in the dependence of the peak heights on the dye−plasmon separation, R. At the smallest R of 1.0 nm, the
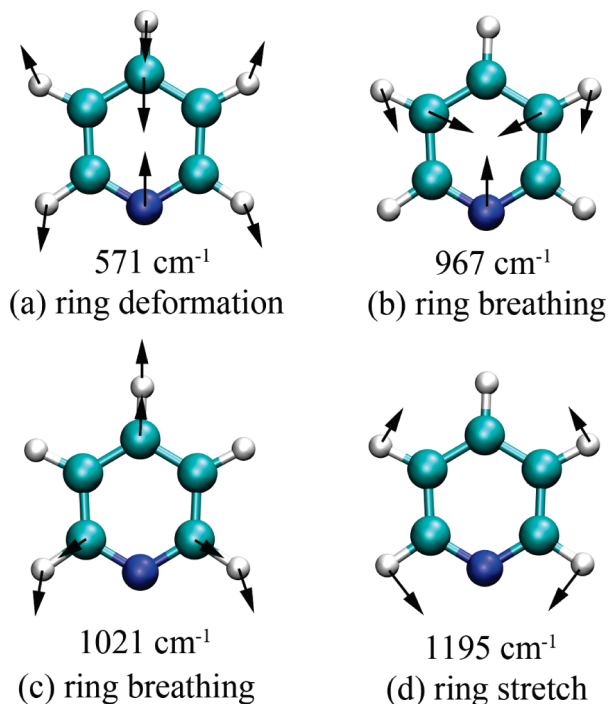
Calculation of Molecular Optical Properties

J. Phys. Chem. C, Vol. 114, No. 34, 2010 **14391**

Figure 8. Plasmon-enhanced vibrational normal modes of pyridine.

1021 cm^{-1} peak is over 5×10^4 in units of 10^{-30} cm^2/sr, equivalent to a 10^4-fold enhancement over the static Raman result of Figure 6 (roughly proportional to $|\lambda_k + 1|^4$, which is a sensible enhancement factor for a silver sphere at 355 nm[45]). By contrast, the enhancement factor dropped to 10^2 when the separation was increased to 5 nm. As expected, the plasmon effect decays much more rapidly in the inner region surrounding the silver sphere than in the outer region in terms of the decreased absolute value of differential Raman cross section for the 1021 cm^{-1} peak. For example, a large decrement of $\sim 3 \times 10^4$ was observed in the Raman signal when R was varied from 1 to 2 nm, whereas a moderate reduction of $\sim 1.8 \times 10^3$ was found when R was increased from 4 to 5 nm. Note that the overall enhancement factor of 10^4 can be further magnified by the so-called chemical and charge transfer enhancements, which change the local chemical environment of the molecule through chemical bonding and intermolecular charge transfer. Within the framework of QM/ED, these two enhancement effects can easily be taken account of with moderate additional computational cost by including the binding site of the silver sphere into the QM level. Nevertheless, the two-dimensional exclusive selectivity of SERS over both incident wavelength and vibrational wavenumber is clearly demonstrated by the three-dimensional contour plot of Raman differential cross section in Figure 9. Despite the distinct absolute values of the cross sections, the two panels exhibit a similar pattern in which only a countable number of vibrational modes are present and all of them have their peaks at 3.49 eV. Moreover, the plasmonic enhancement nearly disappears when the incident photon energy is more than 0.5 eV off the plasmon frequency. In fact, the strength of the Raman signal typically retains more than half of its maximum value within a narrow window of 0.2 eV around the plasmon maximum.

Note that chemical contributions to the SERS enhancement factor have been ignored in this evaluation. Such effects play a role in the SERS spectrum of pyridine, as has been discussed in the past.[16,46] In principle they could be included in our evaluation by adding silver atoms at the point where the pyridine
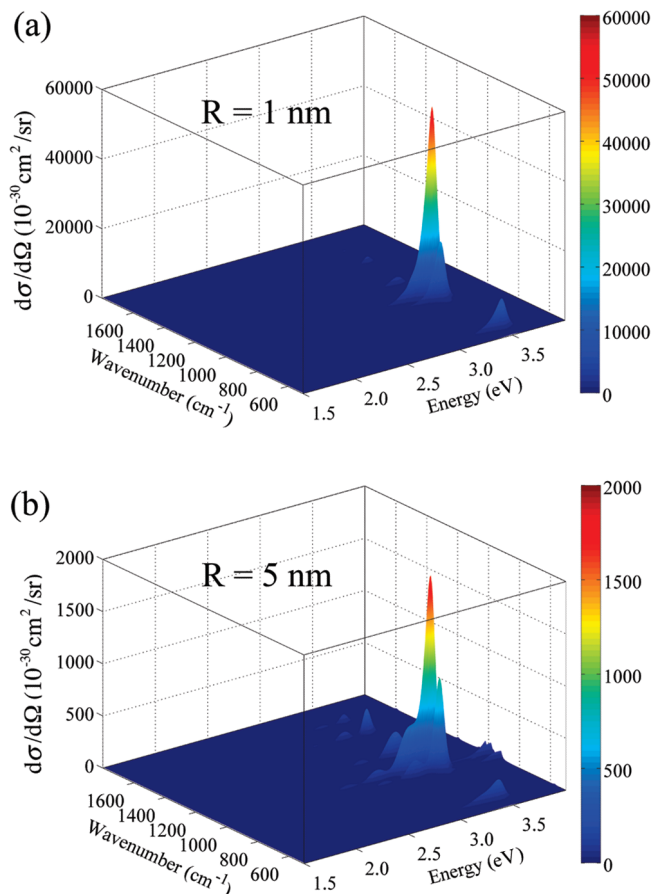

Figure 9. Surface plots of differential Raman cross section of silver-bound pyridine as a function of incident light energy and vibrational mode wavenumber for (a) $R = 1.0$ nm and (b) $R = 5.0$ nm. R is the dye–particle separation.

molecule is adsorbed on the silver particle surface. The present modeling only considered pyridine-particle distances down to 1 nm, so chemical effects should not play a significant role.

4. Discussion and Conclusions

As manifested by our simulated absorption spectrum of the N3 dye and the Raman spectrum of a pyridine molecule, with both molecules near to a 20 nm silver sphere, the hybrid QM/ED method introduced in the present study is demonstrated to provide a bridge spanning the wide gap between quantum mechanics and classical electrodynamics with respect to both length and time scales. Despite the distinct underlying physical mechanisms of the two spectroscopies, experimentally consistent enhancements in the simulated cross sections were observed. Fundamentally, the signal amplification reflects the strong coupling between the wavelike response behavior of the dye molecule's individual electrons and the particle-like collective motion of the silver sphere's dielectric medium. This coupling is sensitive to both their relative location and orientation, in addition to the propagation and polarization directions of the incident light. This shows that the QM/ED method is well suited to study the optical properties of one or several dye molecules near plasmonic nanoparticles. Unlike the conventional frequency domain TDDFT (FD-TDDFT), which requires the diagonalization of a response matrix that is constructed from the occupied–unoccupied orbital pairs and thus grows rapidly with system size,[47] the RT-TDDFT saves significantly on CPU cycles and memory allocation through the use of one-particle wave

function propagations starting from occupied orbitals.[48] In addition, the time scale of the propagation is relatively short due to the assumed damping of the molecular excited state. As a result, the size of a system that can be treated at the QM level in the QM/ED calculations can be expanded to a few hundred atoms, large enough to cover most organic dye molecules of interest. To examine the validity of our assumption of uniform scattered electric field across such a small molecule as N3 and pyridine, a justification calculation was performed on the SERS of pyridine by including the coupling between its quadrupole moment and the electric field gradient. In that calculation, a dye−particle separation of 1.0 nm was chosen for a large electric field gradient near the silver sphere surface. It turns out that the SERS differential cross section was only slightly changed by less than 1%, suggesting that the effect of electric field gradient can be safely ignored in the present study. The FDTD method was selected as the counterpart of RT-TDDFT at ED level, because it proceeds in the real time domain and thus is able to generate the frequency-dependent field-enhancement factor $\lambda(r,\omega)$ in a single simulation through Fourier transformation. Note however that it is convenient to express the coupling between ED and QM via $\lambda(r,\omega)$ in the frequency domain due to the different ways that time is used in FDTD and RT-TDDFT. In FDTD, the time starts when the incident wave leaves its source. On the other hand, the timer in RT-TDDFT is triggered when the incident light actually reaches the molecule. Since we use the frequency domain to interconnect ED and QM, ED methods that work in the frequency domain can be used directly instead of FDTD. For example, the finite element method (FEM)[49] might be used to advantage here as this can circumvent some of the errors in FDTD such as the stair-casing errors that occur in the treatment of curved surfaces. In addition to the flexible coupling scheme between the QM and ED levels of theory, QM/ED allows for an arbitrary number of incident light pulses with any choice of propagation and polarization directions, paving the way to the investigation of time-resolved optical phenomena. Following this successful application of QM/ED for linear optical properties such as absorption and Raman, its extension to nonlinear optical (NLO) materials[50] is anticipated. Other generalizations of this work will arise in the treatment of layers of molecules near metal particles where the self-consistent coupling of the dielectric properties of the molecules to the optical response of the metal particles will be important. In this case it will be necessary to use fields from the QM calculations as input to the ED calculations.

References and Notes

(1) Kirchhoff, G.; Bunsen, R. *Ann. Phys. Chem.* **1860**, *186* (6), 161–189.

(2) Raman, C. V.; Krishnan, K. S. *Nature* **1928**, *121*, 501–502.

(3) Oulton, R. F.; Sorger, V. J.; Zentgraf, T.; Ma, R.-M.; Gladden, C.; Dai, L.; Bartal, G.; Zhang, X. *Nature* **2009**, *461* (7264), 629–632.

(4) Jeanmaire, D. L.; Van Duyne, R. P. *J. Electroanal. Chem.* **1977**, *84* (1), 1–20.

(5) King, F. W.; Van Duyne, R. P.; Schatz, G. C. *J. Chem. Phys.* **1978**, *69* (10), 4472–4481.

(6) Dulić, D.; van der Molen, S. J.; Kudernac, T.; Jonkman, H. T.; de Jong, J. J. D.; Bowden, T. N.; van Esch, J.; Feringa, B. L.; van Wees, B. J. *Phys. Rev. Lett.* **2003**, *91*, 207402.

(7) Grafstrom, S. *J. Appl. Phys.* **2002**, *91* (4), 1717–1753.

(8) Nakanishi, H.; Bishop, K. J. M.; Kowalczyk, B.; Nitzan, A.; Weiss, E. A.; Tretiakov, K. V.; Apodaca, M. M.; Klajn, R.; Stoddart, J. F.; Grzybowski, B. A. *Nature* **2009**, *460* (7253), 371–375.

(9) (a) Viljas, J. K.; Pauly, F.; Cuevas, J. C. *Phys. Rev. B* **2007**, *76*, 033403. (b) Galperin, M.; Nitzan, A. *J. Chem. Phys.* **2006**, *124* (23), 234709–17.

(10) Galperin, M.; Nitzan, A. *Phys. Rev. Lett.* **2005**, *95*, 206802.

(11) Galperin, M.; Tretiak, S. *J. Chem. Phys.* **2008**, *128* (12), 124705–9.

(12) Galperin, M.; Ratner, M. A.; Nitzan, A. *Nano Lett.* **2009**, *9* (2), 758–762.

(13) Zhao, G.; Kozuka, H.; Yoko, T. *Sol. Energy Mater. Sol. Cells* **1997**, *46* (3), 219–231.

(14) Standridge, S. D.; Schatz, G. C.; Hupp, J. T. *J. Am. Chem. Soc.* **2009**, *131* (24), 8407–8409.

(15) Zhao, J.; Pinchuk, A. O.; McMahon, J. M.; Li, S.; Ausman, L. K.; Atkinson, A. L.; Schatz, G. C. *Acc. Chem. Res.* **2008**, *41*, 1710–1720.

(16) Jensen, L.; Aikens, C. M.; Schatz, G. C. *Chem. Soc. Rev.* **2008**, *37* (5), 1061–1073.

(17) Corni, S.; Tomasi, J. *J. Chem. Phys.* **2001**, *114* (8), 3739–3751.

(18) Lopata, K.; Neuhauser, D. *J. Chem. Phys.* **2009**, *130* (10), 104707–7.

(19) Masiello, D.; Schatz, G. C. *J. Chem. Phys.* **2010**, *132*, 064102.

(20) Schrödinger, E. *Phys. Rev.* **1926**, *28* (6), 1049.

(21) Crank, J.; Nicolson, P. *Adv. Comput. Math.* **1996**, *6* (1), 207–226.

(22) Castro, A.; Marques, M. A. L.; Rubio, A. *J. Chem. Phys.* **2004**, *121* (8), 3425–3433.

(23) Castro, A.; Appel, H.; Oliveira, M.; Rozzi, C. A.; Andrade, X.; Lorenzen, F.; Marques, M. A. L.; Gross, E. K. U.; Rubio, A. *Phys. Status Solidi B* **2006**, *243* (11), 2465–2488.

(24) Neugebauer, J.; Reiher, M.; Kind, C.; Hess, B. A. *J. Comput. Chem.* **2002**, *23* (9), 895–910.

(25) Maxwell, J. C. *Philos. Trans. R. Soc. London* **1865**, *155*, 459–512.

(26) Furse, C. M.; Mathur, S. P.; Gandhi, O. P. *IEEE Trans. Microwave Theory Tech.* **1990**, *38* (7), 919–927.

(27) Long, D. A., *Raman Spectroscopy*; McGraw-Hill: New York, 1977.

(28) McMahon, J. M.; Wang, Y.; Sherry, L. J.; Van Duyne, R. P.; Marks, L. D.; Gray, S. K.; Schatz, G. C. *J. Phys. Chem. C* **2009**, *113* (7), 2731–2735.

(29) Johnson, P. B.; Christy, R. W. *Phys. Rev. B* **1972**, *6*, 4370.

(30) Grätzel, M. *J. Photochem. Photobiol., C* **2003**, *4* (2), 145–153.

(31) Nazeeruddin, M. K.; Kay, A.; Rodicio, I.; Humphry-Baker, R.; Mueller, E.; Liska, P.; Vlachopoulos, N.; Graetzel, M. *J. Am. Chem. Soc.* **1993**, *115* (14), 6382–6390.

(32) Hannappel, T.; Burfeindt, B.; Storck, W.; Willig, F. *J. Phys. Chem. B* **1997**, *101* (35), 6799–6802.

(33) Krack, M. *Theor. Chem. Acc.* **2005**, *114* (1), 145–152.

(34) Perdew, J. P.; Burke, K.; Ernzerhof, M. *Phys. Rev. Lett.* **1996**, *77*, 3865.

(35) Woon, D. E.; Dunning, J. T. H. *J. Chem. Phys.* **1994**, *100* (4), 2975–2988.

(36) Genovese, L.; Deutsch, T.; Neelov, A.; Goedecker, S.; Beylkin, G. *J. Chem. Phys.* **2006**, *125* (7), 074105–5.

(37) VandeVondele, J.; Krack, M.; Mohamed, F.; Parrinello, M.; Chassaing, T.; Hutter, J. r. *Comput. Phys. Commun.* **2005**, *167* (2), 103–128.

(38) Gritsenko, O.; Baerends, E. J. *J. Chem. Phys.* **2004**, *121* (2), 655–660.

(39) Gritsenko, O. V.; Schipper, P. R. T.; Baerends, E. J. *Chem. Phys. Lett.* **1999**, *302* (3−4), 199–207.

(40) Duncan, W. R.; Prezhdo, O. V. *Annu. Rev. Phys. Chem.* **2007**, *58* (1), 143–184.

(41) Creighton, J. A. *Notes Rec. R. Soc.* **2010**, *64*, 175–183.

(42) Johnson, A. E.; Myers, A. B. *J. Phys. Chem.* **1996**, *100* (19), 7778–7788.

(43) Nie, S.; Emory, S. R. *Science* **1997**, *275* (5303), 1102–1106.

(44) Arenas, J. F.; Lopez Tocon, I.; Otero, J. C.; Marcos, J. I. *J. Phys. Chem.* **1996**, *100* (22), 9254–9261.

(45) Kelly, K. L.; Coronado, E.; Zhao, L. L.; Schatz, G. C. *J. Phys. Chem. B* **2003**, *107* (3), 668–677.

(46) (a) Lombardi, J. R.; Birke, R. L. *J. Phys. Chem. C* **2008**, *112*, 5605–5617. (b) Morton, S. M.; Jensen, L. *J. Am. Chem. Soc.* **2009**, *131* (11), 4090–4098.

(47) Casida, M. E.; Jamorski, C.; Casida, K. C.; Salahub, D. R. *J. Chem. Phys.* **1998**, *108* (11), 4439–4449.

(48) Takimoto, Y.; Vila, F. D.; Rehr, J. J. *J. Chem. Phys.* **2007**, *127* (15), 154114–10.

(49) Coccioli, R.; Itoh, T.; Pelosi, G.; Silvester, P. P. *IEEE. Trans. Antennas Propag.* **1996**, *38* (6), 34–48.

(50) Eaton, D. F. *Science* **1991**, *253* (5017), 281–287.